IEEE Access
Multidisciplinary | Rapid Review | Open Access Journal

Received June 24, 2021, accepted July 9, 2021, date of publication July 15, 2021, date of current version July 26, 2021.

Digital Object Identifier 10.1109/ACCESS.2021.3097539

Impact of the Current Vector Angle on the Performance of a Synchronous Reluctance Motor With an Axially Laminated Anisotropic Rotor

VALERII ABRAMENKO, ILYA PETROV, JANNE NERG, (Senior Member, IEEE), AND JUHA PYRHÖNEN, (Senior Member, IEEE)

Department of Electrical Engineering, Lappeenranta University of Technology, 53850 Lappeenranta, Finland

Corresponding author: Valerii Abramenko (valerii.abramenko@lut.fi)

This work was supported by the Lappeenranta University of Technology.

ABSTRACT The impact of the current vector angle on the performance of a synchronous reluctance motor (SynRM) with an axially laminated anisotropic (ALA) rotor intended for high-speed applications is studied. The paper shows that the current vector angle not only impacts on the stator winding Joule losses and iron losses, but also strongly influences eddy current losses in the rotor (when the rated torque is produced). The rotor eddy current losses are determined by the flux density harmonics produced by the stator. The air gap flux is affected both by the magnitude and angle of the current vector. However, the rotor surface harmonics are not directly related to the overall flux level (which can be quite low at a high current angle) but depend more on the values of the individual slot current linkages. Considering the dependence of rotor losses on the current vector angle, the most efficient operating point is suggested to be close to 45° or slightly larger, up to 65°, where a compromise between increasing rotor eddy current losses and winding Joule losses and decreasing stator iron losses is found. The eddy current loss distribution between the layers of an ALA rotor is analyzed in detail. With a larger current vector angle, the eddy current losses increase most in the layers close to the d-axis. This is explained by the largest current linkage in the stator slots that are in front of the layers close to the d-axis. The dependence of torque ripple on the current vector angle is also observed. An analysis of rotor and stator high-order harmonics, which determine the torque ripple, is performed.

INDEX TERMS Axially laminated anisotropic rotor, ALASynRM, current vector angle, high speed, high efficiency, inductance difference, rotor harmonics, rotor layers, saliency ratio, synchronous reluctance motor, slot harmonics, space harmonics, torque ripple.

NOMENCLATURE

a	number of parallel branches in a stator winding
B	magnetic flux density (Vs/m^2, T)
f	network frequency (Hz)
I_{RMS}	phase current, RMS (A)
$\boldsymbol{i_s}$	space vector of stator current (A)
i_d, i_q	d-axis and q-axis stator current space vector components (A)
J	current density (A/m^2)
k_{wq}	insulation ratio along q-axis
L_d, L_q	direct- and quadrature-axis inductances (H)
L_{md}, L_{mq}	direct- and quadrature-axis magnetizing inductances (H)
$L_{s\sigma}$	stator winding leakage inductances (H)
n	rotational motor speed (rev/m)
N_s	number of turns in series per phase of stator winding
p	number of pole pairs
R_s	stator resistance (Ω)
R_{mtot}	total reluctance of the magnetic circuit (H^{-1})
T_e	electromagnetic torque (Nm)
U_{ph}	phase voltage, RMS (V)
$\boldsymbol{u_s}$	space vector of the stator voltage (V)
δ_s	load angle of the stator flux linkage (rad), (°)
δ_m	load angle of the air-gap flux linkage (rad), (°)

The associate editor coordinating the review of this manuscript and approving it for publication was Christopher H. T. Lee.

η	efficiency (%)
κ	current vector angle (rad, °)
μ_r	relative permeability
$\tau_{p\nu}$	pole pitch of the ν^{th} harmonic
ν	ordinal of harmonic
$\psi_{\mathbf{s}}$	space vector of the stator magnetic flux linkage (Vs)
$\psi_{\mathbf{m}}$	space vector of the air-gap magnetic flux linkage (Vs)
ψ_{md}, ψ_{mq}	d-axis and q-axis components of the air-gap magnetic flux linkage space vector (Vs)
ω_s	angular frequency of the stator magnetic field (rad/s)
ω_r	angular frequency of the rotor (rad/s)
ALA	axially laminated anisotropic
IM	induction motor
MTPA	maximum torque per ampere
PMSM	permanent magnet synchronous motor
TLA	transversally laminated anisotropic

I. INTRODUCTION

The synchronous reluctance motor with an axially laminated anisotropic rotor (ALASynRM) has been under study for more than six decades [1]–[7], but the machine type has not found a wide practical application so far. This may be related to manufacturing challenges of an ALA rotor. Nevertheless, this motor type is promising and merits further research.

In principle, an ALA rotor is made as a stack of magnetic and nonmagnetic layers. Traditionally, such stacks have simply been bolted on a shaft to compose, e.g., a four-pole rotor. Such a structure provides a significantly larger inductance difference and saliency, and therefore, a better electromagnetic performance potential in comparison with a traditional SynRM that has a transversely laminated anisotropic (TLA) rotor [8]. However, the rotor where the layers are connected with bolts is mechanically fragile. Another problem is that the axial laminations may experience high eddy current losses. If a normal industrial machine was manufactured based on the ALA principle, the rotor should be manufactured from insulated and high-quality sheet materials to obtain a low-rotor-loss design.

In the case of an ALASynRM as a high-speed machine, a fully solid two-pole ALA rotor can be considered. Because of the strong anisotropic properties of a high-speed ALA rotor, the ALASynRM can achieve a higher efficiency than a solid-rotor induction motor (IM) of similar speed and power [4]. Like a solid induction motor rotor, the solid ALA rotor structure with metallic joints between its different layers is electrically highly conducting, and the rotor-surface eddy currents induced by air-gap harmonics can deteriorate the performance of a small-air-gap machine. Therefore, the potential of the ALASynRM to provide a high performance is greater in high-speed applications, where the air gap is made significantly larger to reduce rotor-surface eddy current losses and to provide sufficient cooling conditions.

As an ALASynRM does not require expensive materials, it is a more attractive solution than a permanent magnet synchronous motor (PMSM). High-speed PMSMs are usually implemented with rotor surface magnets. Such an approach makes the motor more expensive. The rotor construction is challenging as the magnets need a strong retaining system. The retaining system is assembled by gluing the magnets and the coating. The magnets tend to move during the assembly, which leads to a balancing problem [9]. A traditional means of retaining the magnets is to use a carbon fiber band, which produces an undesirable thermal insulation on the magnets. The vulnerability of the magnets to high temperatures is a further aspect that complicates the PMSM design. There are magnets capable of withstanding high temperatures (up to 550 °C); however, they are more expensive and have lower remanence than normal-temperature high-energy magnets [10].

So far, the ALASynRM has not often been considered an alternative in high-speed applications because of the challenges in the manufacture of the rotor. However, manufacturing technologies such as hot isostatic pressing, vacuum brazing, and explosion welding allow the ALASynRM to become a competitive high-speed machine. Ideally, the metallurgically joined nonmagnetic and magnetic layers of the rotor can provide a mechanically solid construction offering as high strength as a single-piece solid steel rotor.

As a high-speed machine, a two-pole ALASynRM was analyzed in 1996 [11]. The authors suggested explosion welding as the manufacturing method. The first prototype was built by using vacuum brazing in 1998. In [12], different materials for magnetic and nonmagnetic layers were considered. It was concluded that the rotor materials should have not only high mechanical robustness but preferably also high resistivity to minimize eddy currents. In [12], the motor was rotated at 10000 rpm and 10 Nm for one hour (the rated power was 60 kW). The temperature did not exceed 60 °C. However, at a higher speed and torque, the increase in the rotor temperature can be much larger, and the stress caused by different expansion rates of the materials can deteriorate the motor integrity.

In [13], the ALASynRM was designed taking into account not only the mechanical and electromagnetic characteristics of the magnetic and nonmagnetic materials but also their thermal expansion coefficients. The selected materials S355 and Inconel 718 have thermal expansion coefficients very close to each other but different yield strengths. In [14], the possibility of merging S355 and Inconel 718 by hot isostatic pressing was shown. However, vacuum brazing was not suited for joining of these materials. Therefore, Inconel 600, more suitable for brazing, was used instead of Inconel 718.

In [15]–[19], a four-pole 120 kW, 55000 rpm ALASynRM control was studied. Vector control, precision of the control, and LC filtering to minimize PWM losses were considered. However, manufacturing aspects and mechanical robustness details were omitted, and the geometrical parameters of the motor were not specified.

This paper studies the impact of the current vector angle on the performance of an ALASynRM. The results show that not only the winding Joule losses and the iron losses change at a different orientation of the current vector but also the rotor eddy-current losses are strongly affected because the high-order flux density harmonics have different amplitudes at different current vector angles, while the torque is kept constant.

The content of the paper is the following. Section II provides the initial data for the research in brief. Section III presents an observation of the phenomenon under study and the theory development. In Section IV, the distribution of eddy current losses between the layers of the ALA rotor is studied. Section V considers the dependence of torque ripple on the current vector angle κ and the relation of the torque ripple to the stator and rotor harmonics of the air-gap flux density. The practical contributions of the study are discussed in Section VI. Section VII concludes the findings of the paper.

II. INITIAL DATA

The initial data for the study were taken from [13]. The 12 kW ALASynRM was designed based on the same-power IM with a solid rotor equipped with copper end rings. The stator was the same and only the rotor was replaced with an ALA rotor. The detailed data of the stator and rotor of the referenced IM can be found in [13]. In the ALASynRM, the rotor materials used in the ferromagnetic and nonmagnetic layers are S355J0 and Inconel 718, respectively. These materials have similar thermal expansion coefficients, which makes them suitable for rotor manufacture with heat treatment methods. The relevant properties of the materials are given in Table 1.

In [13] it was shown that an ALASynRM (designed taking the heat treatment manufacturing methods into consideration) controlled with the maximum torque per ampere (MTPA) strategy provides a higher efficiency than the reference IM with either a smooth solid rotor with copper end rings or a slitted solid rotor with copper end rings. The ALASynRM rotor has 47 layers: 24 nonmagnetic Inconel 718 layers and 22 magnetic S355 layers of 2 mm thickness, and in the middle, one magnetic S355J0 layer of 6.5 mm thickness. The stator steel used in the analysis is NO20. The geometry of the motor is shown in Fig. 1, and its performance values are given in Table 2. This ALASynRM is used in the present study.

The 12 kW ALASynRM was analyzed with the 2D FEM simulation in the Altair Flux software. The validity of the 2D FEM simulation of the IM and ALASynRM was discussed in [13]. This approach is suitable in the present case, because only the ALASynRM is investigated and possible errors caused by neglecting the end effect will be present in all simulated cases, which makes the comparative study equitable. To avoid the impact of the circulating third-order stator currents and the corresponding rotor eddy current losses [20], the stator winding was connected in star. The quality of the mesh was selected to be such that a further increase in the mesh quality would not produce any noticeable increase in the calculation precision. This was shown in [14].

Another important aspect in the FEM simulation is the time step applied. An erroneously selected time step may result in a significant omission of losses caused by high-order harmonics. According to the Whittaker–Nyquist–Kotelnikov–Shannon theorem, to take into account the impact of a certain harmonic, the time step should be shorter than half of the time period of the harmonic under consideration. However, in general, the harmonics with higher ordinals have a lower amplitude. Therefore, the time step can be selected in such

TABLE 1. Relevant properties of S355J0 and Inconel 718.

Parameter	Value	
	S355J0	Inconel 718
Initial relative permeability	≈1000	1.001
Saturation flux density (T)	1.9	–
Electrical resistivity (Ohm·m)	$25.7 \cdot 10^{-8}$	$124.9 \cdot 10^{-8}$
Temperature coefficient of resistivity (1/K)	0.0038	0.00024
Thermal expansion coefficient (1/K)	$12.5 \cdot 10^{-6}$	$12.8 \cdot 10^{-6}$
Yield strength (MPa)	355	1100
Ultimate tensile strength (MPa)	520	1375
Mass density (kg/m^3)	7830	8190

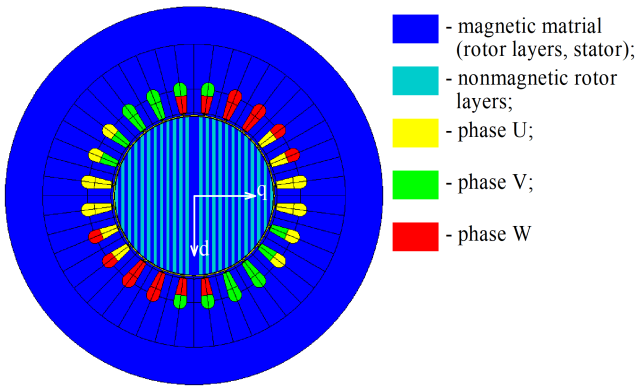

FIGURE 1. Geometry of the ALASynRM under study.

TABLE 2. Performance values of the 12 kW ALASynRM at 400 Hz supply and MTPA control.

Parameter	Value
Output power (kW)	12
Speed (rpm)	24000
Torque (Nm)	4.775
Peak-to-peak torque ripple (Nm)	2.07
Rated phase current RMS (A)	28.15
d-axis synchronous inductance (mH)	4.43
q-axis synchronous inductance (mH)	0.34
Inductance difference (mH)	4.09
Saliency, L_d/L_q	13.13
Stator winding losses (W)	92.67
Stator iron losses (W)	175.53
Rotor Joule losses (W)	205.62
Total losses (W)	473.81
Efficiency (%)	96.2
Power factor	0.674

a way that the impact of the most significant high-order harmonics is taken into account, while the harmonics that have an insignificant impact on the performance estimation are neglected. Here, Fig. 2 shows the loss components of the motor (Fig. 1) under study as a function of time step. The MTPA control strategy was applied. In the present case, the time step of 1/400 of the fundamental period was selected as a compromise between the calculation accuracy and the expense of computing time. The difference in eddy current losses is less than 7% between the selected time step and the time step with which the impact of all harmonics is maximally taken into account (with 800 or more points per electrical period of stator fundamental). The data on the selected time step are listed in Table 3.

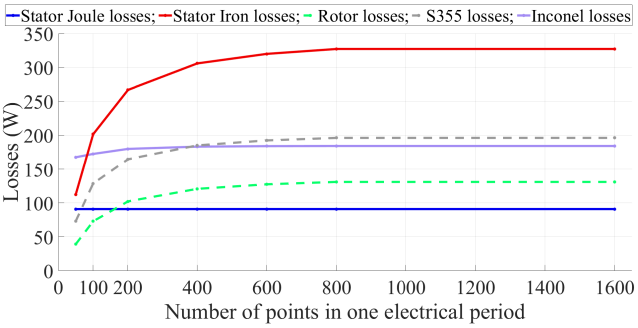

FIGURE 2. Results of loss component calculation as a function of the number of time steps per stator fundamental.

TABLE 3. Data on the selected time step.

Parameter	Value
Fundamental frequency (Hz)	400
Fundamental period (ms)	2.5
Selected time step (μs)	6.25
Covered harmonic range	up to 80 kHz (order 1 – 200)

III. IMPACT OF THE CURRENT VECTOR ANGLE ON THE PERFORMANCE OF THE ALASynRM

This section represents the core of the study. The known theory of the impact of the current vector angle is described. The ALASynRM is analyzed with different values of the current vector angle κ, and the key findings are presented in the section. Based on the results, an additional theory is developed. A detailed study of the rotor loss distribution between the layers is reported.

A. ORIGINAL THEORY

Increasing the current vector angle (κ in Fig. 3) from 45° to 85° decreases the magnetization of the machine, while the current absolute value has to grow to produce the same torque. This can be seen by analyzing the equation for the SynRM electromagnetic torque in per-unit values [21]:

$$T_{em} = i_q\psi_{md} - i_d\psi_{mq} = i_q i_d \left(L_{md} - L_{mq}\right) = \frac{1}{2} i_s^2 \sin(2\kappa) \left(L_{md} - L_{mq}\right), \quad (1)$$

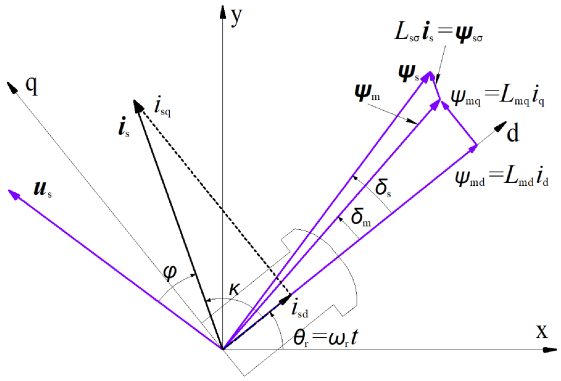

FIGURE 3. Conceptual vector diagram of the SynRM.

where i_d is the d-axis current, i_q is the q-axis current, ψ_d is the d-axis flux linkage, ψ_q is the q-axis flux linkage, L_d is the d-axis inductance, and L_q is the q-axis inductance.

Increasing the current, naturally, results in higher Joule losses in the stator winding. The winding Joule losses directly correspond to the square of the stator current. In theory, the MTPA control results in the minimum current when κ equals 45°. The current vector amplitude has to increase to reach the same torque if κ is larger or smaller than 45°.

The iron losses diminish with a larger κ because the magnetizing (d-axis) current, and as a result, the fundamental of the air-gap flux density, decrease even though the total current vector amplitude increases. This is explained by the fact that in a SynRM, the air gap flux linkage vector (ψ_m) is mainly determined by the d-axis current (i_{sd}) as the d-axis has a much higher permeance (or a larger inductance, L_d) than the q-axis. From the conceptual vector diagram (Fig. 3), it can be seen that the d-axis flux linkage component (ψ_d) contributes to the magnetizing flux linkage ($\psi_{\mathbf{m}}$) much more strongly than the q-axis armature reaction (ψ_q). In Fig. 4, the flux density in the 12 kW ALASynRM is shown at different current vector angles κ. In all cases, the current amplitude was adjusted to produce the rated torque (Fig. 5). Thus, with an increasing κ and the corresponding increase in the current amplitude needed for the rated torque, the fundamental flux density in the motor decreases.

In traditional SynRMs with a TLA rotor, possible changes in the rotor losses are usually not considered when the direction of the current vector is varied. The reason for this is that the iron losses produced by the fundamental flux density are zero as the rotor runs in synchronism, while the iron losses caused by the stator winding and the permeance harmonics are quite efficiently mitigated in the transversally laminated rotor steel sheets. In addition, the maximum rotational speed of a SynRM with a TLA rotor is significantly limited because of the constructional weakness of the lacelike rotor laminations [22]. At low speeds, the eddy currents produced by the stator spatial harmonics are less essential than at high speeds. Therefore, the optimal operating point is usually found with

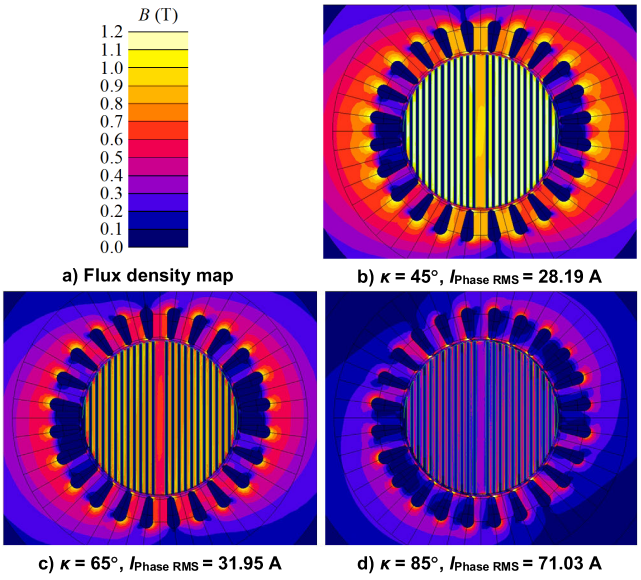

FIGURE 4. Flux density distribution at different current vector angles and at the rated load.

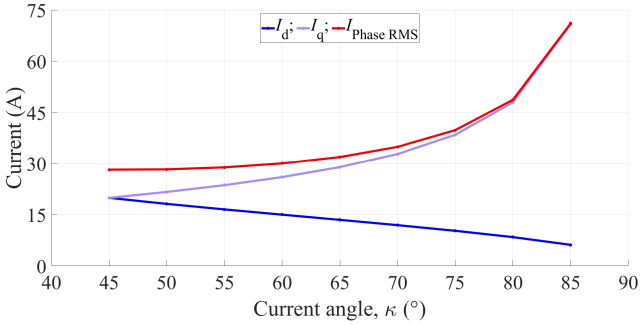

FIGURE 5. Current components and the stator current as a function of current vector angle when producing rated torque.

κ slightly higher than 45° and far from 90°, where the d-axis magnetization is totally lost.

B. OBSERVATION OF THE NEW PHENOMENON

The 12 kW ALASynRM under study has a well-conducting rotor with strong magnetic anisotropy. As mentioned above, the simulation was implemented so that with κ increasing from 45° to 85°, the current amplitude was adjusted to provide the rated torque. In Fig. 6, the dependence of losses on the current vector angle is given. The stator winding Joule losses grow when the total current increases (Fig. 5), while the stator iron losses decrease when the d-axis current (Fig. 5), and therefore, the total magnetization decrease (Fig. 4). However, the rotor eddy current losses in both the magnetic and nonmagnetic layers increase with a larger κ. This is explained in the current section.

In Fig. 7, the air-gap flux density at the same time instances is provided for the current vector angles of 45°, 65°, and 85°. The curves include fundamental, stator, and rotor air-gap flux density harmonics. However, the rotor eddy current losses in synchronous machines are caused only by the high-order

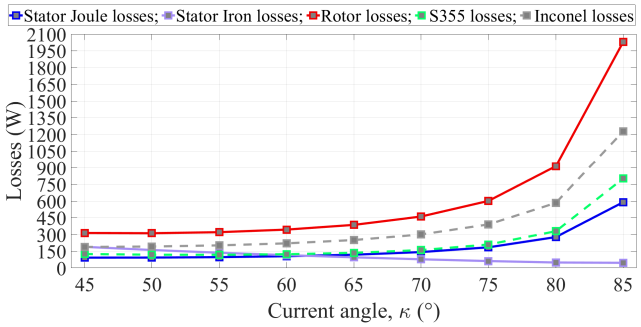

FIGURE 6. Different ALASynRM losses as a function of stator current vector angle keeping a constant torque.

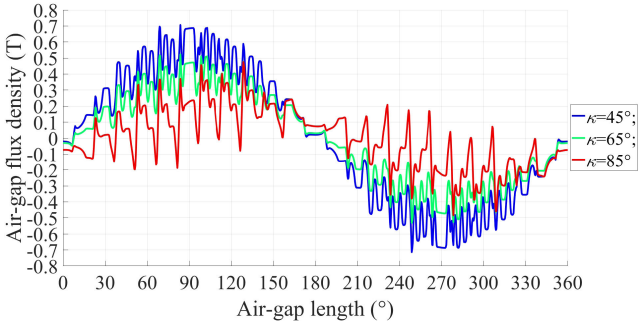

FIGURE 7. Air-gap flux density distribution for cases with current vector angles of 45°, 65°, and 85°.

stator current linkage and the stator permeance harmonics. In Fig. 8, the air-gap flux density harmonics produced solely by the stator side are provided for several current vector angles. The separation of stator harmonics was made by a two-dimensional Fast Fourier transform [23]. Logically, the fundamental flux density decreases as the magnetizing current decreases with an increasing κ. However, the high-order flux density harmonics grow, which poses a need for an explanatory theory. For the sake of readability, the harmonic spectrum only up to the 50th harmonic is considered here, even though harmonics of higher order are also present and are addressed in Section VI with the explanation of torque ripple.

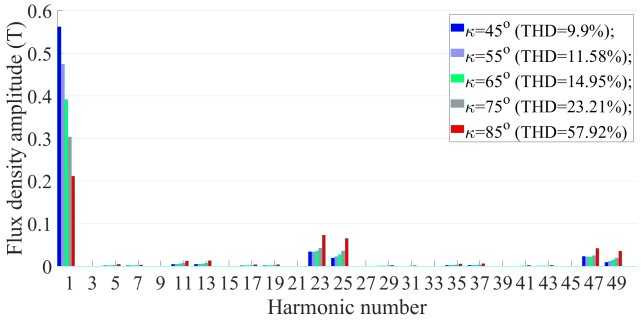

FIGURE 8. Stator-side-produced harmonics of the air-gap flux density at different current vector angles. THD denotes total harmonic distortion calculated taking into account only the stator-produced harmonics and excluding the rotor-produced ones.

The significant growth in the current amplitude (and consequently, the growth in the stator current linkage and high-order harmonics, Figs. 5, 8) at κ-values larger than 75° is explained by the drop of the power factor (Fig. 9). When κ starts to increase from 45°, the power factor is first growing because the current vector is turned closer to the voltage vector. However, when κ reaches 80°, the q-axis armature reaction becomes stronger and the d-axis armature reaction becomes weaker to such an extent that the voltage vector (which is 90° ahead of the stator flux linkage vector) is ahead of the current vector strongly enough to start to deteriorate the power factor. In addition, the leakage flux linkage is proportional to the current magnitude, and therefore, a larger current itself has a negative impact on the power factor. As it can be seen from Fig. 9, the d- and q-axis inductances do not change much with the current vector angle, because the ALASynRM operates below the saturation level at all κ-values under consideration (Fig. 4).

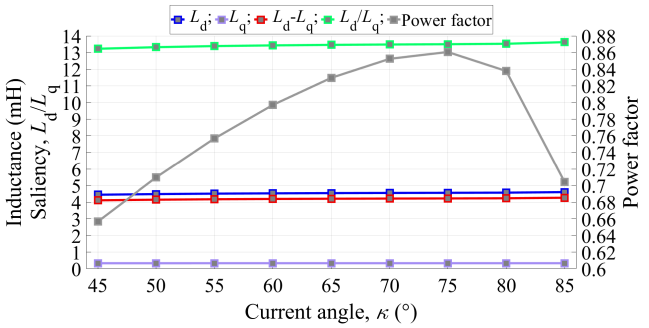

FIGURE 9. Inductances and power factor as functions of current vector angle.

C. EXPLANATION OF THE RESULTS AND THEORY DEVELOPMENT

The high-order flux density harmonics and loss behavior are explained as follows. With the growth of κ, the current linkage tends to magnetize more the low-permeance q-axis and less the high-permeance d-axis. As a result, the total reluctance of the rotor for the main flux grows. This can be evaluated by (1). The total reluctance of the ALASynRM magnetic circuit as a function of current vector angle is shown in Fig. 10

$$R_{\mathrm{mtot}} = \frac{(k_{\mathrm{w}}N_{\mathrm{s}})^2/a}{(U_{\mathrm{rms}} - I_{\mathrm{rms}}R_{\mathrm{s}})/I_{\mathrm{rms}}/(2\pi f)}, \tag{2}$$

where k_{w} is the winding factor, N_{s} is the number of turns in series per phase of stator winding, a is the number of parallel branches, U_{rms} is the RMS phase voltage induced in the winding, I_{rms} is the RMS phase current, R_{s} is the phase winding resistance, and f is the supply frequency.

In other words, the total rotor permeance decreases for the fundamental magnetic flux. However, the high-order harmonics have a shorter path through the rotor than the fundamental flux density because of their smaller pole pitch, which can be

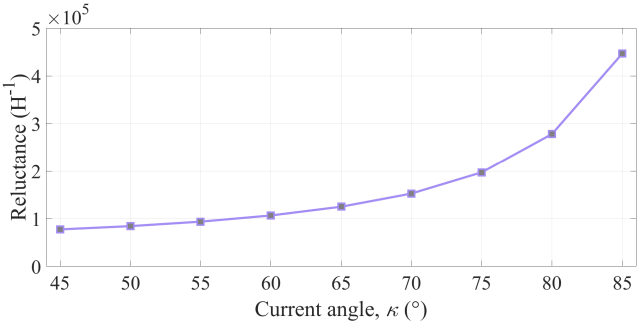

FIGURE 10. ALASynRM reluctance as a function of current vector angle.

determined with the following equation:

$$\tau_{\mathrm{p}\nu} = \frac{\pi D_{\mathrm{s}}}{2p\,|\nu|}, \tag{3}$$

where $\tau_{\mathrm{p}\nu}$ is the pole pitch of the harmonic, D_{s} is the inner diameter of the stator, and ν is the harmonic ordinal.

It means that the variation in the overall rotor permeance for the fundamental does not affect the high-order harmonics to the same extent it affects the fundamental. Therefore, the change in κ does not impact on the reluctance met by the high-order harmonics as much as the one met by the fundamental. As the high-order harmonics travel on the rotor surface, the change in the rotor position relative to the rotor magnetization does not significantly affect the amount of magnetic and nonmagnetic materials through which the harmonics travel. As it was mentioned above, to keep the same torque, the total stator current has to grow with κ (Fig. 5), which means that the total current linkage also increases. It results in larger high-order harmonics of the air-gap flux density and an increase in rotor eddy current losses.

To verify the proposed explanation, tests with a solid rotor and different permeabilities were implemented. This approach allows to exclude any impact of the rotor anisotropy on the stator harmonics. A motor version with a homogeneous rotor was supplied by the same currents that were supplied in the ALASynRM with different κ-values, while the permeability was adjusted to obtain the same terminal voltages as in the ALASynRM. The dependences of voltages and permeabilities of the solid rotor on κ are shown in Fig. 11. There is no anisotropy in the solid rotor, and therefore, κ is called a pseudo-current angle. Here, the pseudo-current angle simply implies the parameter values (voltage and currents) taken from the cases with the ALASynRM for the corresponding κ cases. The air-gap flux density harmonics with the homogeneous rotor are shown in Fig. 12.

The spectrum analyses of the air-gap flux density with the ALA rotor (Fig. 8) and the homogeneous rotor (Fig. 12) show that the high-order stator harmonics behave similarly as a function of κ. For a more detailed analysis, the stator winding and slot harmonic amplitudes as functions of κ are shown in Figs. 13 and 14, respectively, for both the ALA and homogeneous rotors in the whole range of κ variation.

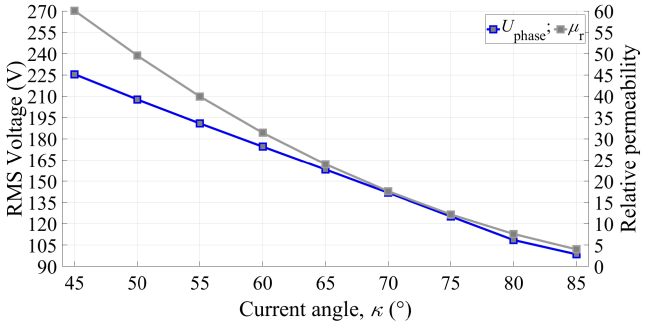

FIGURE 11. Voltage and relative permeability of the solid rotor as a function of pseudo-current vector angle.

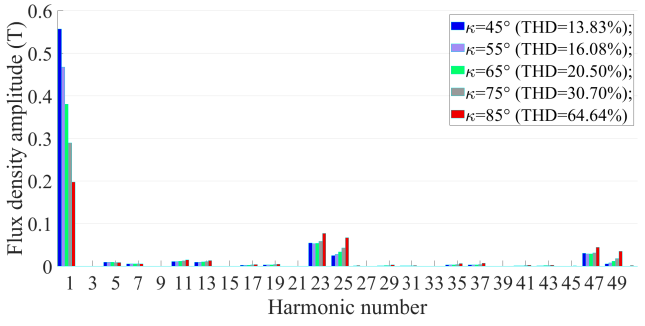

FIGURE 12. Spectrum analysis of the air-gap flux density with the homogeneous rotor. Different κ-values mean different terminal voltage and rotor permeability in accordance with Fig. 11.

With the ALA rotor, the amplitudes of the harmonics are smaller than those with the homogeneous rotor, because the homogeneous rotor was simulated as electrically nonconducting, while the ALA rotor has electrically conducting layers. The induced eddy currents in the ALA rotor oppose the stator harmonics, which therefore have lower amplitudes compared with the case with the homogeneous rotor. Another reason for the smaller amplitude of the high-order stator harmonics with an ALA rotor is the presence of torque, which makes the flux lines travel through the stator slots more in the tangential direction, while with an isotropic rotor the flux lines travel almost completely in the normal direction. This impacts on the total flux distribution in the slots, and consequently, the high-order stator harmonics.

The main mismatch between the ALA rotor and isotropic rotor cases occurs in the behavior of the fifth and seventh harmonics (Fig. 13). These harmonics are lower with the isotropic rotor and rise with the ALA rotor when κ increases. The reduction in those harmonics (especially the fifth) with an isotropic rotor is explained by the fact that their path is larger compared with the paths of the 11^{th} and 13^{th} harmonics winding harmonics or slot harmonics. Therefore, the rotor reluctance constitutes a significant part of the path (and correspondingly, reluctance) for the fifth and seventh harmonics. The growing dependence of the fifth and seventh harmonics on κ in the case of the ALA rotor is explained, again, by the electrically conducting layers. The conducting material expels these harmonics on the surface of the rotor,

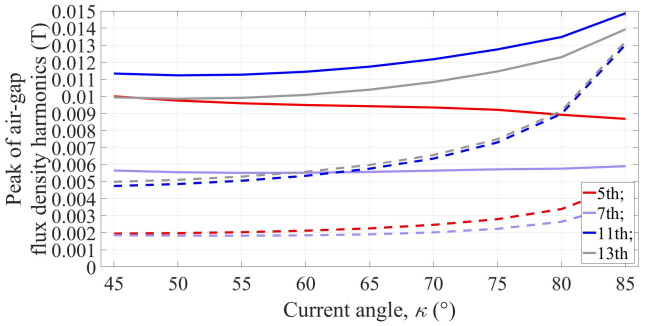

FIGURE 13. Winding harmonics as a function of current vector angle (or pseudo-current vector angle). The solid lines represent the case with an isotropic rotor, and the dashed lines represent the case with the ALA rotor.

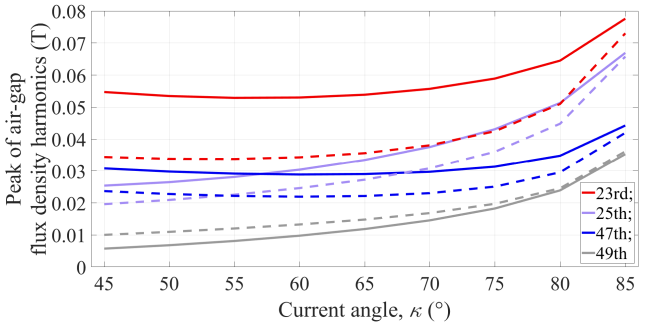

FIGURE 14. Stator permeance harmonics as a function of current vector angle (or pseudo-current vector angle). The solid lines represent the case with an isotropic rotor, and the dashed lines indicate the case with the ALA rotor.

which makes their amplitude less dependent on the magnetic conductivity of the rotor and more dependent on the total current, which increases with a larger κ.

The growth of high-order stator harmonics with an increasing κ can also be explained with an equivalent magnetic circuit (Fig. 15). With a larger κ, the winding current linkage θ_{W} and reluctance of the rotor medium R_{medium} increase. The largest part of the fundamental flux has to flow through

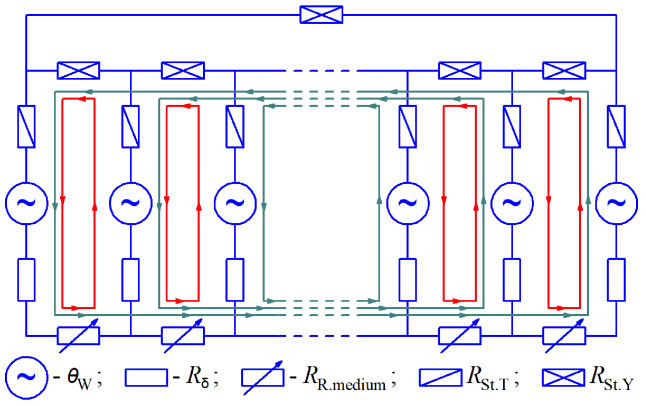

FIGURE 15. Equivalent magnetic circuit of the ALASynRM. θ_{W} is a source of current linkage in the winding. $R_{\text{St.Y}}$ is the stator yoke reluctance within a stator slot pitch area, $R_{\text{St.T}}$ is the stator tooth reluctance, R_{leak} is the stator tooth leakage reluctance, R_{δ} is the air-gap reluctance, and R_{medium} is the reluctance of the rotor medium within a stator slot pitch.

a significant amount of the rotor medium, and the reluctance for the fundamental magnetomotive force increases significantly with a larger κ. Therefore, the fundamental flux becomes smaller despite the growth in the total current linkage. However, the stator slot harmonics have a relatively short circulation path. The total reluctance for the slot harmonics is insignificantly affected by κ, and their amplitudes are strongly affected by the current linkage, which increases with κ.

IV. DISTRIBUTION OF ROTOR EDDY CURRENT LOSSES

The distribution of the rotor eddy current losses between the layers at different values of κ deserves additional consideration (Fig. 16). There is a clear trend that the losses grow toward the layers positioned closer to the d-axis with a larger κ. The only exceptions are the layers in the middle. Such a nonconformity is related to the thicker middle layer, which affects the eddy current distribution in it itself and in the layers nearby. The magnetic and nonmagnetic layers have different penetration depths; an attempt to explain the dependence of eddy current loss distribution on the thicknesses and electromagnetic characteristics of the layers was made in [14]. One of the further research questions is related to the impact of κ on the eddy current loss distribution between the layers.

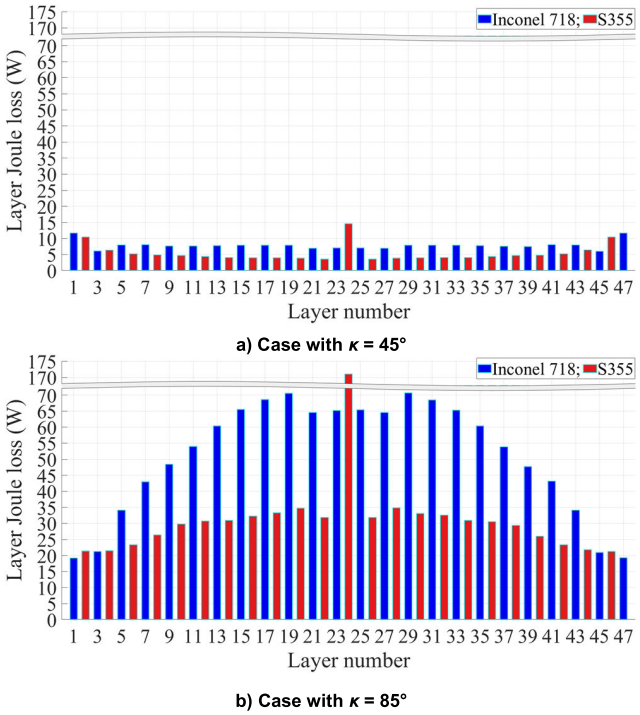

FIGURE 16. Loss distribution in the individual rotor layers. A wide ferromagnetic middle layer.

To avoid the impact of a larger thickness of the middle layer on the loss distribution, additional simulations were made in which the middle layer was divided into three layers, where the middle one of 2.5 mm was assigned to the nonmagnetic and the other two on the sides to the magnetic material. This particular design case is considered hereafter in terms of current density distribution at different κ. For the sake of readability, only the cases with κ of 45°, 65°, and 85° are presented. The losses in the layers grow toward the layers positioned close to the d-axis with larger κ (Fig. 17). This trend can be explained by the fact that the largest distortion of the stator flux takes place closer to the d-axis when κ is high. Fig. 18 shows the air-gap flux density distribution produced solely by the stator-related harmonics, which are the winding and permeance harmonics. Here, the rotor layers were assigned to the electrically nonconducting materials (S355 and Inconel 718 but with infinite resistivity) to obtain the stator flux density harmonics not affected by the rotor eddy currents. The air-gap flux densities from the stator harmonics were obtained by a two-dimensional Fast Fourier transform, where the stator and rotor harmonics were separated, and only the targeted stator harmonics were used for

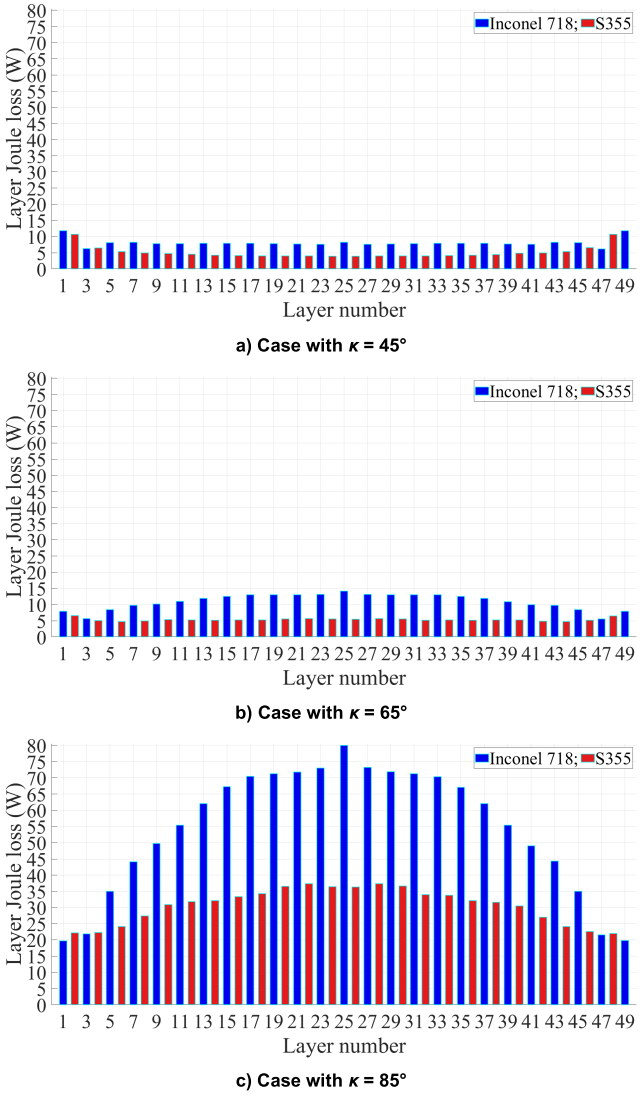

FIGURE 17. Loss distribution in individual rotor layers. Middle layer divided into thinner layers.

the curve reproduction. The curves are built for the same particular time instant, which corresponds to the rotor position in Fig. 1; however, at the other time instants the curve patterns are similar to the ones shown in Fig. 18.

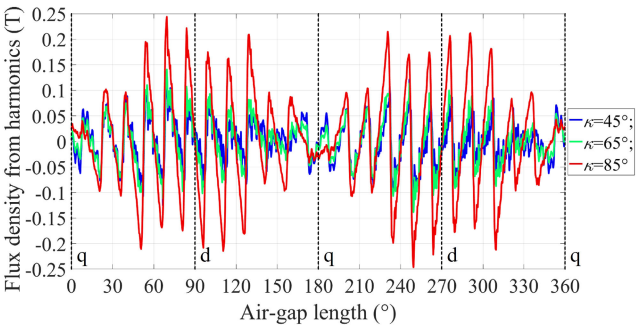

FIGURE 18. Flux density in the air gap close to the rotor surface created by the stator winding and the permeance harmonics alone. The rotor position is indicated by the d- and q-axis orientation, which corresponds to Fig. 1, and the air-gap angle starts to be measured from the q-axis counterclockwise.

In Fig. 19, the current density in the stator slots and rotor with κ of 45°, 65°, and 85° is shown. The peak of the current density is larger with a larger κ, but for a comparative analysis, the range of the current density in the scale bar was set to be the same for all the cases under study. The rotor current density distribution is in agreement with the data in Figs. 17 and 18.

The losses in the rotor of a distributed winding machine with proper short pitching mostly depend on the stator slotting effect because the winding harmonics are minimized [23]. In principle, the rotor losses are caused by stator permeance harmonics. However, there is an additional source of rotor eddy-current losses that originates from the stator side and is related to the tooth tip flux leakage. According to Fig. 20, there is a stator tooth tip flux leakage between two neighboring tooth tips, which travels through the air gap [24]. However, if the current in the slots is large enough, then this tooth tip flux leakage can easily reach the rotor region and induce significant eddy current losses in the rotor layers. The amplitude of the tooth tip flux leakage in different slots depends on the total current in the slot and on the relative position of the rotor over the slot with the current. The slots with a larger current linkage generate a stronger tooth tip leakage flux that is finally found in a form of a stator harmonic.

In order to cover the main trend of the loss distribution between the layers, the following aspects should be considered. The first is the distribution of layer surfaces on the rotor periphery. For example, the surface of layers number one and 49 on the rotor sides covers a much larger proportion of the rotor periphery than the layers close to the d-axis. The second is the value of the current linkage in the slots, to which the slot harmonics and tooth tip leakage value are proportional. These finally affect the flux density harmonics in the air gap. The third is the rotor position relative to the peak of the total current linkage.

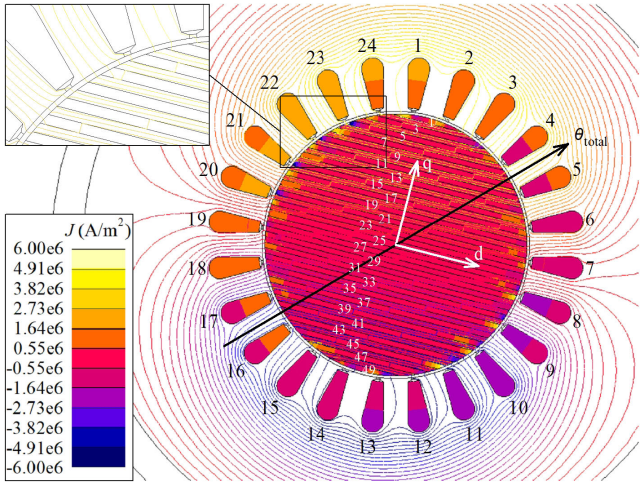

a) Case with κ = 45°

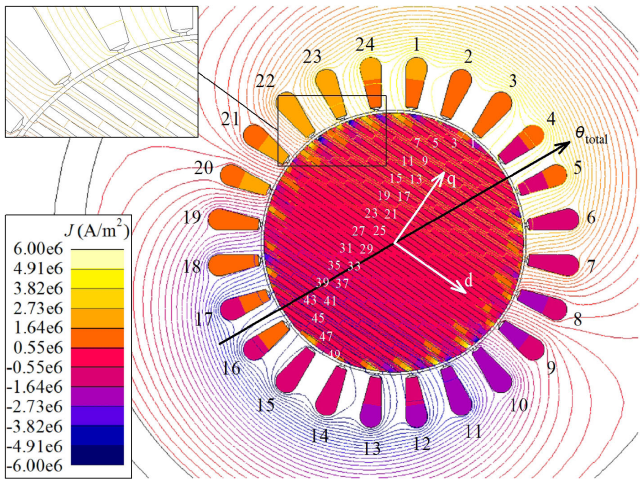

b) Case with κ = 65°

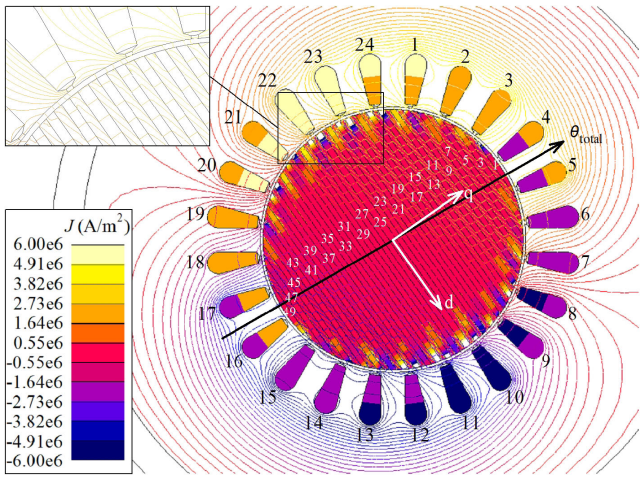

c) Case with κ = 85°

FIGURE 19. Current density distribution in the ALA rotor and slots with different current vector angles. The odd layers of the rotor are numbered.

In Fig. 19, the current density in the slots directly represents the current linkage distribution and its orientation relative to the rotor position. All the cases were considered at the time instants when the vector of the total current linkage

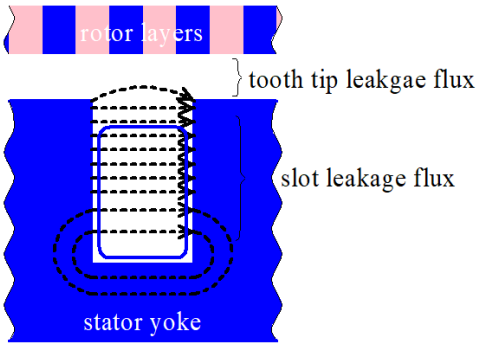

FIGURE 20. Leakage flux component of a coil winding in a slot.

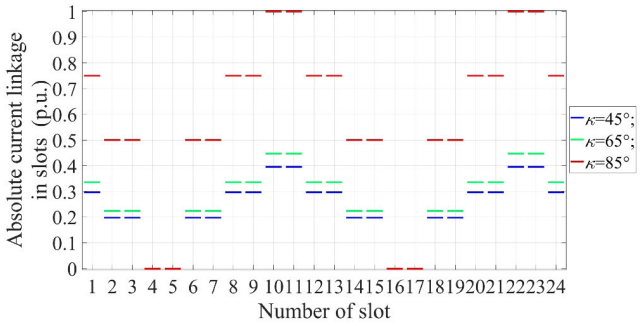

FIGURE 21. Current linkage in the stator slots in per unit values. The peak of current linkage in the slot with the current vector angle of 85° is assumed as 1 per unit.

θ_{tot} is in the same direction and formed when the peak of current occurs in the phase positioned in the following slots: 10, 11 and 22, 23 as well as in the half of the slots 8, 9, 12, 13 and 20, 21, 24, 1 (because of short pitching in the winding). In addition, in Fig. 21 the absolute current linkage in slots is shown in per unit values, where 1 p.u. is assumed to be equal to the maximum slot current linkage when κ is 85°. The difference in the current linkage with a different κ results from reaching the same torque when a different current vector control angle is applied.

Thus, if we compare the current linkage in the slots that are facing the layers close to the d-axis, for example, the layers 22–26, we can see the following. In the case of $\kappa = 45°$, the layers 22–26 are facing the slots 7, 8 and 19, 20. The current linkages in these slots are about 0.2 and 0.3 p.u. (Fig. 21). Then, in the case of $\kappa = 65°$, the layers 22–26 are facing the slots 8–10 and 20–22, where the current linkages are about 0.34 and 0.45 p.u. Finally, in the case of $\kappa = 85°$, the layers 22–26 are in front of the slots 9–11 and 21–23, where the current linkages are about 0.75 and 1 p.u. The layers 22–26 are located in front of the slots with a larger current linkage when κ is increased, which results in a stronger tooth tip leakage penetrating these layers, and consequently, in the growth of loss in these layers with an increasing κ.

Considering the layers 1, 2 and 48, 49, the current linkage in the slots in front of these layers also differs with κ. For example, with $\kappa = 45°$ these layers are facing the areas of the slots 24, 1, 2, 3 and 12, 13, 14, 15, where the current linkages are about 0.3, 0.3, 0.2, and 0.2 p.u., respectively. However, with $\kappa = 65°$, these layers are in the areas of the slots 1–5 and 13–17, where the current linkages are about 0.34, 0.22, 0.22, 0, and 0 p.u., respectively, which results in lower losses in the layers under consideration than with the slot current linkages in the case of $\kappa = 45°$ (Fig. 17a and b). With $\kappa = 85°$, the layers 1, 2 and 48, 49 are in front of slots (3–6 and 15–18) with the current linkages 0.5, 0, 0, and 0.5 p.u., which induces a much stronger eddy current compared with the cases with a lower κ (Fig. 17c).

Thus, with an increasing κ, not only the total current linkage increases but also the rotor position changes relative to the slots where the current linkage is different. In Fig. 19, the flux lines in the areas of the slots with the largest current linkage are zoomed. With a larger κ, the slot leakage and tooth tip leakage fluxes increase, which is especially noticeable in the case with $\kappa = 85°$.

V. IMPACT OF THE CURRENT VECTOR ANGLE ON THE TORQUE RIPPLE

The torque curves at κ values of 45°, 65°, and 85° are provided in Fig. 22, and the dependence of the torque ripple on κ is illustrated in Fig. 23. It is clear that at the beginning of an increase in κ, the torque ripple becomes smaller and then increases when κ gets larger than 70°. In principle, the torque ripple can be described by high-order torque harmonics (Fig. 24). In the present case, the dependence of peak-to-peak torque ripple on κ coincides with the dependence of high-order harmonics of torque on κ, especially with the 72nd torque harmonic. These high-order torque harmonics are the result of the interaction of the stator and rotor high-order flux density harmonics with adjacent ordinals. For example, the 72nd harmonic of torque is produced by the 71st and/or 73rd flux density harmonics, while these harmonics must be produced by both the stator and rotor sides to make a corresponding torque component.

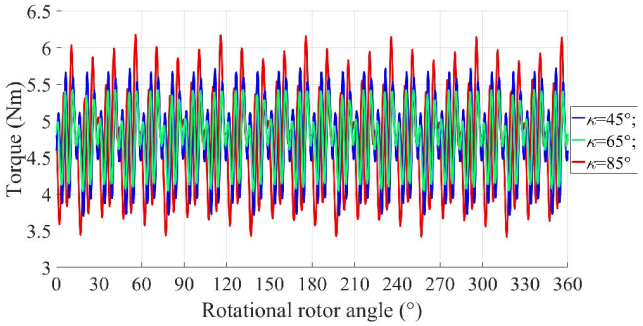

FIGURE 22. Torque as a function of rotational angle at the rated speed of the ALASynRM under study at current vector angles of 45°, 65°, 85°.

In Figs. 25 and 26, the harmonics produced by the stator and rotor sides are illustrated. With a larger κ, most of the high-order stator-side flux density harmonics rise (only the 23rd, 47th, 71st, and 95th harmonics slightly decrease

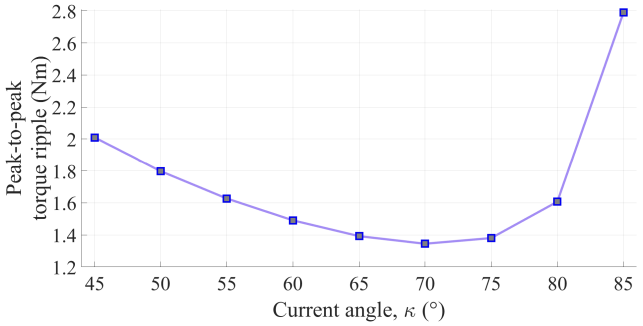

FIGURE 23. Peak-to-peak torque ripple as a function of current vector angle.

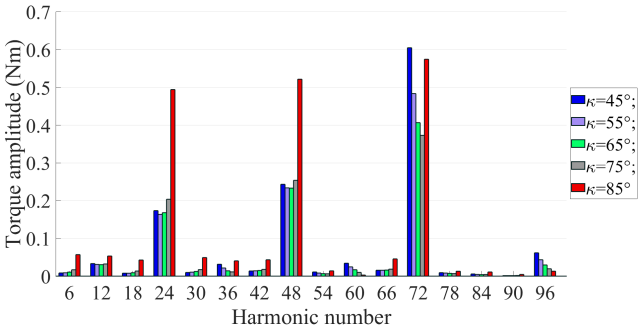

FIGURE 24. High-order torque harmonics at the current vector angles under consideration.

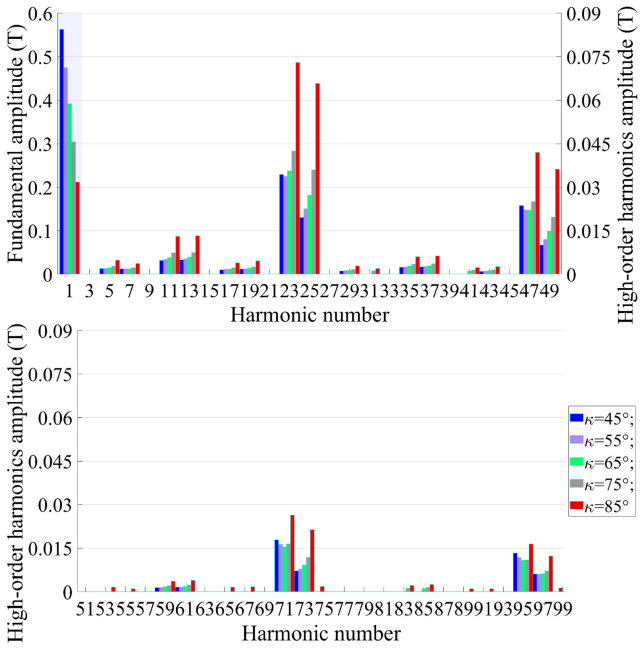

FIGURE 25. Stator-side-produced harmonics of the air-gap flux density at the current vector angles under consideration.

at the beginning of an increase in κ, while with a further κ increase they also become larger); the reason for the increase in the high-order stator-side harmonic was discussed in previous sections. The rotor-side flux density harmonics become smaller with a larger κ. This is explained by the

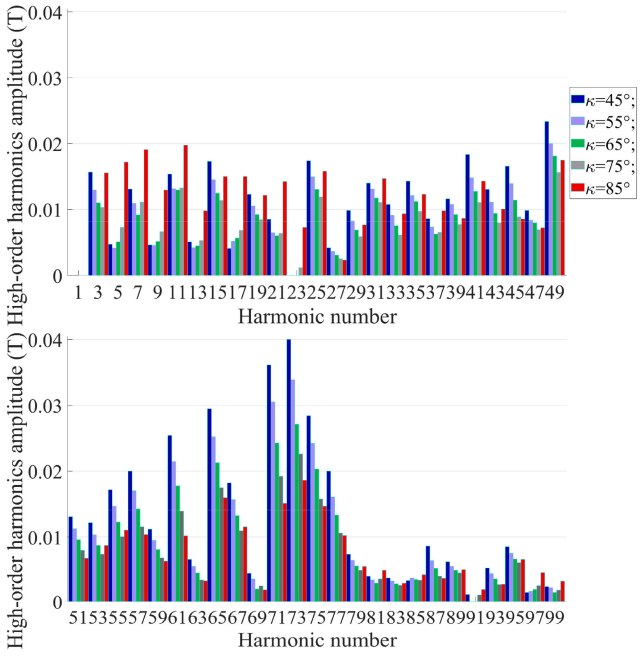

FIGURE 26. Rotor-side-produced harmonics of the air-gap flux density at the current vector angles considered (rotor harmonics are those which are absent in the case of a perfect isotropic rotor).

reduction in the total level of the flux density of the machine as the rotor does not have a source of flux itself but can only distort the flux that flows from the stator. Thus, such an increasing trend in the stator-side flux density harmonics and a decreasing trend in the rotor-side harmonics produce corresponding torque harmonics and torque ripple, which has a parabolic dependence on κ (Fig. 23).

The rotor-produced harmonics have a correlation with the rotor geometry. Assuming an ideal case with a sinusoidal flux density distribution produced by the stator (Fig. 27a), the resulting flux should be determined by the rotor permeance distribution. If we consider that the magnetic layers have a permeance of one and the permeance of nonmagnetic layers is zero, then the distribution of the permeance along the rotor periphery can be represented as in Fig. 27b. Basically, the graph corresponds to the peripherical length of the magnetic and nonmagnetic layers. In this ideal case, the resulting flux should have a form shown in Fig. 27c. The spectrum analysis of such a flux waveform is provided in Fig. 28. It can be seen how the high-order rotor-produced harmonics in the motor (Fig. 26) correlate with the rotor flux density harmonics in an ideal case (Fig. 28). For example, the most dominant rotor harmonics 71st, 73rd, and 75th (Fig. 26) correspond to the largest high-order rotor harmonics in an ideal case (Fig. 28), while similarly, the high-order rotor harmonics of lower values (e.g., 13th, 23rd, 69th etc. in Fig. 26) correspond to the smallest harmonics of the same order in an ideal case (Fig. 28). If the real and ideal cases of the rotor-produced harmonics are compared, it can be noticed that the correlation between them in per unit values is not perfect. This is explained by the fact that in the real

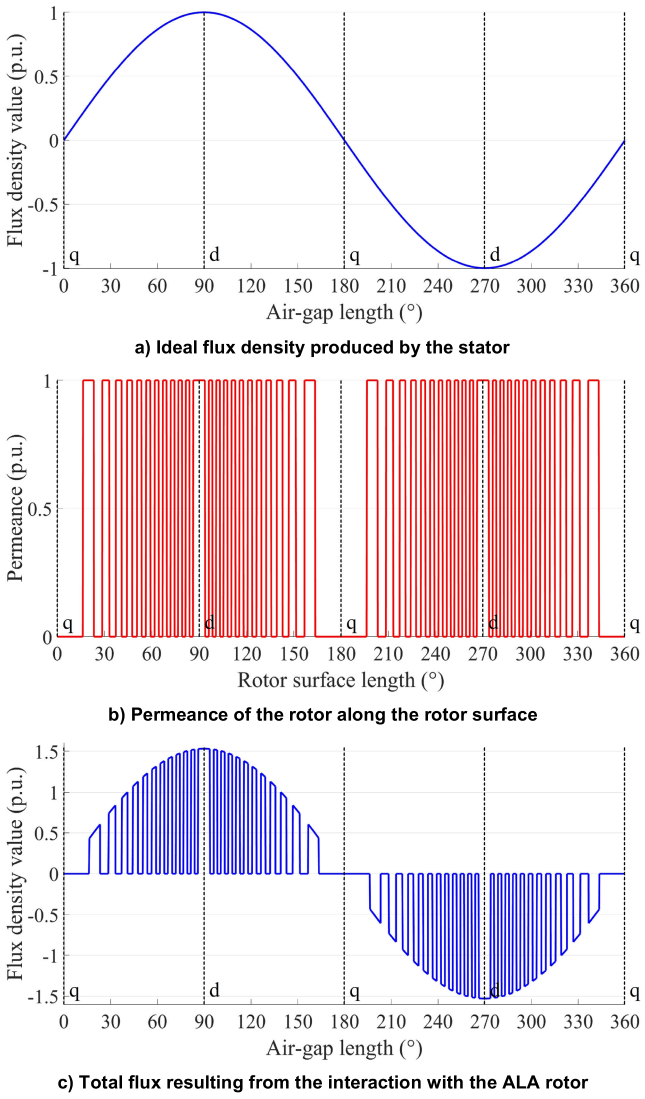

a) Ideal flux density produced by the stator

b) Permeance of the rotor along the rotor surface

c) Total flux resulting from the interaction with the ALA rotor

FIGURE 27. Ideal case of flux density distribution along the rotor periphery when the d-axis is magnetized. In p.u. values, 1 is assumed to be permeance along magnetically conducting layers and 0 along magnetically nonconducting layers. It is assumed that all the stator flux is distributed in the rotor magnetic layers so that the area below the sine half-waves (a) is equal to the area below the half-waves of rotor-distorted signal. It results in a flux density in the middle layer of slightly higher than 1.5 p.u.

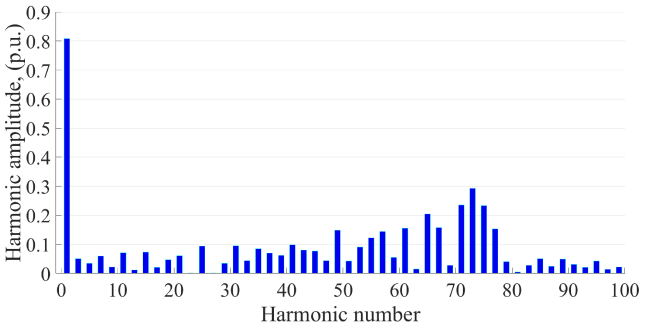

FIGURE 28. Fourier analysis of the flux density distribution along the rotor periphery in an ideal case (Fig. 27c).

case, the flux density from the rotor side is not sinusoidal but distorted with stator winding and permeance harmonics. Moreover, the real permeance differs from the one in Fig. 27b, because the layers have different sizes and not identical values of permeability. However, the similarity is clear enough to conclude the origin of the main rotor-side harmonics.

It should be noted that this logic does not explain the case with κ of 85°, where certain high-order rotor harmonics (e.g. 25th, 49th) are larger than in the cases with κ of lower values, which results in a significant increase in the corresponding torque harmonics. It is because with κ of 85°, a large proportion of flux flows through the q-axis. When κ is lower than 80°, the largest proportion of flux flows through the d-axis even though the q-axis current can be significantly larger than the d-axis current. For example, flux lines in Fig. 19 show that in the cases with κ of 45° and 65° the flux mainly magnetizes the d-axis, while only with κ of 85° the flux is noticeably shifted toward the q-axis. Therefore, the rotor harmonics at κ of 85° do not correlate with the harmonics in Fig. 28 (where it is assumed that all magnetization is oriented along the d-axis), because the interaction of the flux with the rotor q-axis is different from the interaction with the rotor d-axis.

Another point deserving attention is that the numbers of the most dominating rotor harmonics are not close to the number of rotor layers. The number of magnetic and nonmagnetic areas along the rotor surface (not to be confused with the number of layers) is 46 each. However, as it can be seen from Fig. 28, the 46th rotor harmonic is not the dominating one. It is related to the fact that the periodicity of the magnetic and nonmagnetic segments along the rotor periphery is not the same. It is clear that the peripheral length of the layers close to the q-axis is larger than the peripheral length of the layers close to the d-axis when the rotor segments have about the same width. Basically, the pattern of the surface permeance determines the rotor flux density harmonics.

It is worth mentioning that the eddy currents induced in the rotor by high-order stator-side space harmonics have a negligible impact on the rotor-produced harmonics of the air-gap flux density. It was proven by comparing the air-gap flux density analysis with electrically conducting and nonconducting layers. The difference is slight.

VI. DISCUSSION

The phenomenon under study indicates that a high-quality design or precise optimization of an ALASynRM requires not only consideration of conventional motor parameters, such as the geometrical size of the machine parts, the number of winding turns, and materials, but also the control strategy applied. In the present case of a 12 kW ALASynRM, the highest efficiency is achieved at the current vector angle of about 55° (Fig. 29) by reducing iron losses in the stator core, while the stator winding Joule losses and the rotor eddy-current losses increase to a lower extent compared

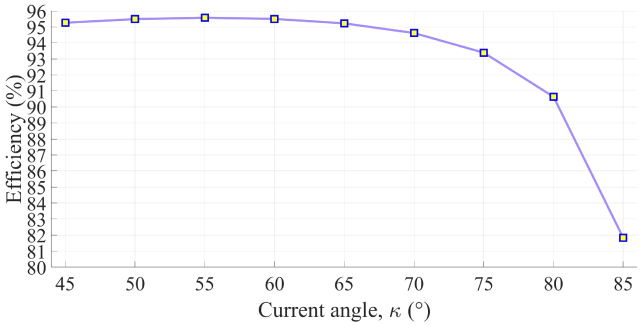

FIGURE 29. Efficiency of the studied ALASynRM as a function of current vector angle.

with the stator iron losses in that range of current vector angle (Fig. 6).

Based on the results obtained, it can be stated that the MTPA control strategy provides the minimum rotor eddy current losses (and as known, the minimum stator winding Joule losses). Usually, in high-speed machines, the stator winding Joule losses are significantly lower than the stator iron and rotor eddy current losses, because the limit of the maximum current density in the stator winding does not allow a further increase in the air-gap length to reduce the stator iron and rotor eddy-current losses. Such observations suggest that when a fast design of an ALASynRM is required, the design can be implemented with the MTPA (or just slightly larger than a 45° current vector angle) control condition with adjustment of the air gap keeping the current density in the stator winding below the allowable limit. In addition, the MTPA is the most favorable control strategy from the viewpoint of the thermal behavior of the motor.

If some other control strategies are to be applied, they may involve a significant sacrifice of efficiency. For example, if the fastest torque control (fastest torque response) is required, the value of current vector angle should be 85.6° according to the equation [21]

$$\kappa = \arctan\frac{L_\mathrm{d}}{L_\mathrm{q}}. \tag{4}$$

Similarly, the maximum power factor control is implemented with $\kappa = 75°$ according to Fig. 9 or equation [21]

$$\kappa = \arctan\sqrt{\frac{L_\mathrm{d}}{L_\mathrm{q}}}. \tag{5}$$

Neither $\kappa = 75°$ nor $\kappa = 85°$ provide operation at the highest or even close to the highest efficiency mostly because of the significant increase in the rotor eddy current losses in the solid ALA rotor. These findings should be taken into account when deciding upon the control strategy.

If torque ripple is of high importance, the stator- and rotor-produced harmonics in the air-gap flux density should be analyzed together. A certain harmonic of torque can be minimized by reducing the corresponding stator and/or rotor harmonics. As the rotor harmonics are related to the rotor geometry, the thickness of the magnetic and nonmagnetic layers can be adjusted to avoid the dominance of a certain torque harmonic when the stator geometry is fixed. Thus, it was shown in [14] that the minimum torque ripple in an ALASynRM is achieved with a certain thickness of rotor layers (not with the smallest thickness but an optimal one). Even though in high-speed machines the impact of torque ripple is usually not of high importance as it is effectively damped by rotor inertia, torque ripple might be related, e.g., to a certain acoustic noise component. When the human environment factor is considered, minimization of a certain torque component can make sense. In addition, the torque ripple can be reduced by selecting a certain current angle at which the interaction of the dominating stator and rotor high-order harmonics is at the minimum.

VII. CONCLUSION

The study shows the impact of the current vector angle κ on the ALASynRM performance. With a larger current vector angle (an increase in the q-axis current and a decrease in the d-axis current), the magnetization of the motor decreases. However, the high-order flux density harmonics increase because they travel through a shorter path compared with the path of the fundamental flux density. This results in larger eddy current losses in the rotor. The increase in the rotor eddy current losses is especially pronounced with large values of current angle, above 70°. For example, when κ changes from 45° to 65°, the rotor losses increase by 23% (from 314 W to 387 W), whereas when κ changes from 45° to 85°, the rotor losses increase by 546% (from 314 W to 2030 W). This emphasizes the dependence of efficiency on the current angle. In the range of κ from 45° to 65°, the efficiency varies somewhat between 95.2% and 95.6%, while with κ above 65°, the efficiency deteriorates significantly by dropping slightly below 82% at κ of 85°.

The distribution of losses between the layers of the ALA rotor also changes with larger current vector angles. The largest losses are concentrated in the layers closest to the d-axis, because they are located in front of the stator slots where the current linkage is increased most significantly. The large current linkage in the slots results in stronger stator slot flux density harmonics, which reach the rotor surface and induce eddy currents. The phenomenon should be taken into account in the design of an ALASynRM. In Section VII, it was suggested that the best operating point can be found close to the MTPA control strategy (a current vector angle of 45° or slightly larger).

The torque ripple as a function of current angle was also analyzed. In the present case, the maximum reduction in torque ripple is slightly more than 30% compared with the MTPA operating point and found at $\kappa = 75°$. κ impacts on the amplitudes of both the stator and rotor flux density harmonics; therefore, the torque ripple also differs with a change in κ. In a similar manner as a stator can be optimized to reduce certain stator-side flux density harmonics, a rotor can be adjusted to reduce specific rotor-side harmonics to avoid or minimize particular torque harmonics.

REFERENCES

[1] A. Cruickshank, R. Menzies, and A. Anderson, "Axially laminated anisotropic rotors for reluctance motors," *Proc. Inst. Elect. Eng.*, vol. 113, no. 12, pp. 2058–2060, 1966.
[2] A. J. O. Cruickshank, A. F. Anderson, and R. W. Menzies, "Theory and performance of reluctance motors with axially laminated anisotropic rotors," *Proc. Inst. Elect. Eng.*, vol. 118, no. 7, pp. 887–894, 1971.
[3] D. Platt, "Reluctance motor with strong rotor anisotropy," *IEEE Trans. Ind. Appl.*, vol. 28, no. 3, pp. 652–658, May 1992.
[4] D. A. Staton, T. J. E. Miller, and S. E. Wood, "Maximising the saliency ratio of the synchronous reluctance motor," *IEE Proc. B (Electr. Power Appl.)*, vol. 140, no. 4, pp. 249–259, 1993.
[5] T. Matsuo and T. A. Lipo, "Rotor design optimization of synchronous reluctance machine," *IEEE Trans. Energy Convers.*, vol. 9, no. 2, pp. 359–365, Jun. 1994.
[6] B. J. Chalmers and L. Musaba, "Design and field-weakening performance of a synchronous reluctance motor with axially laminated rotor," *IEEE Trans. Ind. Appl.*, vol. 34, no. 5, pp. 1035–1041, Sep. 1998.
[7] C. L. Gu, L. R. Li, K. R. Shao, and Y. Q. Xiang, "Anisotropic finite element computation of high density axially-laminated rotor reluctance machine," *IEEE Trans. Magn.*, vol. 30, no. 5, pp. 3679–3682, Sep. 1994.
[8] I. Boldea, Z. X. Fu, and S. A. Nasar, "Performance evaluation of axially-laminated anisotropic (ALA) rotor reluctance synchronous motors," *IEEE Trans. Ind. Appl.*, vol. 30, no. 4, pp. 977–985, Jul. 1994.
[9] L. Wu, Q. Sun, Y. Zhu, and X. Ye, "Dynamic balance consistency analysis of permanent magnet synchronous motor rotor based on centrifugal force," in *Proc. 22nd Int. Conf. Electr. Mach. Syst. (ICEMS)*, Harbin, China, Aug. 2019, pp. 1–5.
[10] D. Gerada, A. Mebarki, N. L. Brown, and C. Gerada, "High-speed electrical machines: Technologies, trends, and developments," *IEEE Trans. Ind. Electron.*, vol. 61, no. 6, pp. 2946–2959, Jun. 2014.
[11] H. Hofmann and S. R. Sanders, "Synchronous reluctance motor/alternator for flywheel energy storage systems," in *Proc. Power Electron. Transp.*, Dearborn, MI, USA, Oct. 1996, pp. 199–206.
[12] H. Hofmann and S. R. Sanders, "High-speed synchronous reluctance machine with minimized rotor losses," *IEEE Trans. Ind. Appl.*, vol. 36, no. 2, pp. 531–539, Mar. 2000.
[13] V. Abramenko, I. Petrov, J. Nerg, and J. Pyrhonen, "Synchronous reluctance motors with an axially laminated anisotropic rotor as an alternative in high-speed applications," *IEEE Access*, vol. 8, pp. 29149–29158, 2020.
[14] V. Abramenko, J. Nerg, I. Petrov, and J. Pyrhonen, "Influence of magnetic and nonmagnetic layers in an axially laminated anisotropic rotor of a high-speed synchronous reluctance motor including manufacturing aspects," *IEEE Access*, vol. 8, pp. 117377–117389, 2020.
[15] J.-D. Park, H. Hofmann, and C. Khalizadeh, "Feedforward control of high-speed solid-rotor synchronous reluctance machines with rotor dynamics model," in *Proc. Conf. Rec. IEEE Ind. Appl. Conf., 39th IAS Annu. Meeting.*, Seattle, WA, USA, Oct. 2004, p. 298.
[16] J.-D. Park, C. Khalizadeh, and H. Hofmann, "Design and control of high-speed solid-rotor synchronous reluctance drive with three-phase LC filter," in *Proc. 14th IAS Annu. Meeting. Conf. Rec. Ind. Appl. Conf.*, Oct. 2005, pp. 715–722.
[17] J.-D. Park, C. Kalev, and H. F. Hofmann, "Control of high-speed solid-rotor synchronous reluctance motor/generator for flywheel-based uninterruptible power supplies," *IEEE Trans. Ind. Electron.*, vol. 55, no. 8, pp. 3038–3046, Aug. 2008.
[18] J.-D. Park, C. Kalev, and H. F. Hofmann, "Analysis and reduction of time harmonic rotor loss in solid-rotor synchronous reluctance drive," *IEEE Trans. Power Electron.*, vol. 23, no. 2, pp. 985–992, Mar. 2008.
[19] J. D. Park, C. Kalev, and H. Hofmann, "Modeling and control of solid-rotor synchronous reluctance machines based on rotor flux dynamics," *IEEE Trans. Magn.*, vol. 44, no. 12, pp. 4639–4647, Dec. 2008.
[20] V. Abramenko, I. Petrov, J. Nerg, and J. Pyrhonen, "Third-order harmonics in synchronous reluctance motors with an axially laminated anisotropic rotor and their impact on the motor losses," *IEEE Access*, vol. 8, pp. 152870–152880, 2020.
[21] J. Pyrhonen, V. Hrabovcova and R. S. Semken, *Electrical Machine Drives Control: An Introduction*. Chichester, U.K.: Wiley, 2016.
[22] A. Credo, G. Fabri, M. Villani, and M. Popescu, "Adopting the topology optimization in the design of high-speed synchronous reluctance motors for electric vehicles," *IEEE Trans. Ind. Appl.*, vol. 56, no. 5, pp. 5429–5438, Sep. 2020.
[23] C. Di, I. Petrov, and J. Pyrhönen, "Extraction of rotor eddy-current harmonic losses in high-speed solid-rotor induction machines by an improved virtual permanent magnet harmonic machine model," *IEEE Access*, vol. 7, pp. 27746–27755, 2019.
[24] J. Pyrhonen, T. Jokinen and V. Hrabovcova, *Design of Rotating Electrical Machines*, 2nd ed. Hoboken, NJ, USA: Wiley, 2013.

VALERII ABRAMENKO received the Specialist degree in electrical drives and automation of industrial installations from South Ural State University (SUSU), Chelyabinsk, Russia, in 2014, and the M.Sc. degree in electrical engineering jointly from SUSU and the Lappeenranta University of Technology (LUT), Lappeenranta, Finland, in 2017.

He is currently a Researcher with the Department of Electrical Engineering, LUT. His research interest includes high-efficient synchronous motors.

ILYA PETROV received the D.Sc. degree from the Lappeenranta University of Technology (LUT), Finland, in 2015. He is currently a Research Fellow at the Department of Electrical Engineering, LUT.

JANNE NERG (Senior Member, IEEE) received the M.Sc. degree in electrical engineering, the Licentiate of Science (Technology) degree, and the D.Sc. (Technology) degree from the Lappeenranta University of Technology (LUT), Lappeenranta, Finland, in 1996, 1998, and 2000, respectively.

He is currently an Associate Professor with the Department of Electrical Engineering, LUT. His research interest includes the field of electrical machines and drives, especially in electromagnetic and thermal modeling and design of electromagnetic devices.

JUHA PYRHÖNEN (Senior Member, IEEE) was born in Kuusankoski, Finland, in 1957. He received the D.Sc. degree from the Lappeenranta University of Technology (LUT), Finland, in 1991.

He became a Professor of electrical machines and drives at LUT, in 1997. He is engaged in research and development of electric motors and power-electronic-controlled drives. He has wide experience in the research and development of special electric drives for distributed power production, traction, and high-speed applications. Permanent magnet materials and applying them in machines play an important role in his research. He is also researching new carbon-based materials for electrical machines.